Composite Structures 268 (2021) 113964

Contents lists available at ScienceDirect

Composite Structures

journal homepage: www.elsevier.com/locate/compstruct

Systematic approach for finite element analysis of thermoplastic impregnated 3D filament winding structures – General concept and first validation results

Jonathan Haas [a,*], Oktay Nedim Hassan [a], Björn Beck [a], Luise Kärger [b], Frank Henning [a,b]

[a] Fraunhofer Institute for Chemical Technology, Department of Polymer Engineering, Joseph-von-Fraunhofer-Str. 7, 76327 Pfinztal, Germany
[b] Karlsruhe Institute of Technology, Institute of Vehicle System Technology, Rintheimer Querallee 2, 76131 Karlsruhe, Germany

ARTICLE INFO

Keywords:
3D filament winding
Thermoplastic composites
Finite element analysis
Structural simulation

ABSTRACT

This work presents a systematic procedure for the detailed, mesoscopic Finite Element simulation of 3D filament wound fiber skeletons with thermoplastic impregnation. First, relevant structural constituents of thermoplastic fiber skeletons are identified and mechanically characterized by means of specially adapted test methods and specimens. In the next step, the mechanical behavior of the structural constituents is simulated in separate FE models, so-called sub-models. This includes the selection, implementation and parametrization of suitable material models. After that, a Finite Element model for a simple demonstrator fiber skeleton is created, the so-called main model, into which the sub-models are integrated. Finally, the simulation results of the main model are compared to mechanical tests of the demonstrator fiber skeleton. The main model developed in this work allows a precise calculation of the maximum bearable load and a good representation of the delamination process occurring before rupture.

1. Introduction

A promising perspective to open up further lightweight potential in structural components is the use of polymer materials with local continuous fiber reinforcements. This approach is already established in different large-scale production processes of the automotive industry. One of the key issues in this context is the fiber-suitable draping of continuous fiber semi-finished products under consideration of geometric specifications and load path orientations. Since the employed semi-finished products usually have a flat geometry (e.g. thermoplastic tapes, pre-impregnated fabrics), drapability and consequently freedom of design is often restricted, especially in complex three-dimensional applications.

The use of modern robot-based 3D filament winding processes combined with flexible continuous yarns, as practiced in context of the 3D Skeleton Winding technology (3DSW), enables more flexible fiber positioning and thus extends the range of applications for structural plastic components with local continuous fiber reinforcement. 3D filament winding processes are used to manufacture topology optimized composite structures, so-called fiber skeletons, by winding a thermoplastic or thermoset impregnated continuous yarn onto a winding tool. The winding tool determines the shape of the fiber skeleton as it fixes the position of the fiber deflection points during the winding process. If required, inserts can be attached to the winding tool, which become a part of the fiber skeleton and can serve as a bearing or load introduction point. After its manufacture, the fiber skeleton is overmolded in an injection molding process, as shown in the 3DSW process in Fig. 1, hence serving as local continuous fiber reinforcement of a structural injection molded part. Fig. 1 also indicates the impregnation step which precedes the 3D filament winding process. An exemplary structural 3DSW demonstrator component before and after overmolding is shown Fig. 2.

While facilitating the design and manufacture of local continuous fiber reinforcements, the 3DSW technology presents new challenges in the field of structural dimensioning. A realistic estimation of the fiber skeleton's mechanical behavior by means of calculation models is crucial, since the manufacture of testable skeleton prototypes usually involves numerous cost and time intensive adjustments of the winding tool and the robot trajectory programming. Discrete models of filament wound lattice structures enable precise stiffness estimations of large fiber skeletons under different load types with reasonable modeling and computational effort, as comprehensively

* Corresponding author.
E-mail address: jonathan.haas@ict.fraunhofer.de (J. Haas).

https://doi.org/10.1016/j.compstruct.2021.113964
Received 4 November 2020; Revised 13 February 2021; Accepted 8 April 2021
Available online 13 April 2021
0263-8223/© 2021 The Authors. Published by Elsevier Ltd.
This is an open access article under the CC BY license (http://creativecommons.org/licenses/by/4.0/).

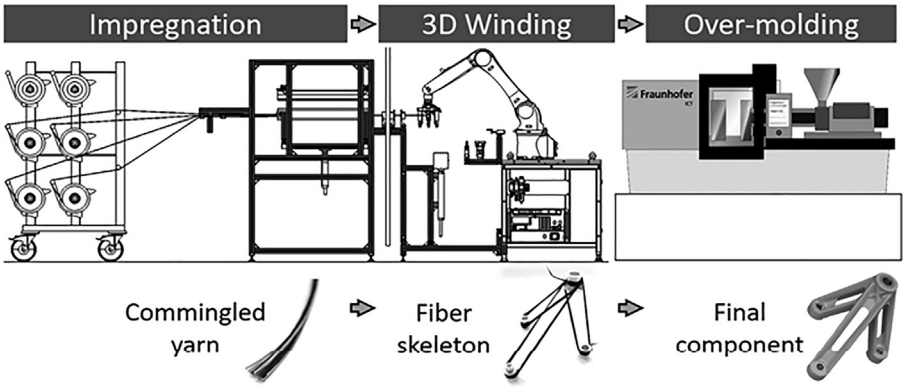

Fig. 1. Process of the 3DSW technology, modified from [1].

Fig. 2. Generic 3DSW demonstrator – fiber skeleton (left) and continuous fiber reinforced part (right).

reviewed by Morozov et al. [2]. Especially discrete FE models, in which ribs are represented by rod or beam elements and fiber deflection points are modeled as rigid connections between these elements, are still frequently used for the mechanical evaluation of large filament wound lattices [3,4]. However, this kind of model is not sufficiently precise to consider failure mechanisms within wound reinforcement structures whose failure is typically initiated by stress peaks in complex winding patterns at the fiber deflection points [1,5]. Therefore, more detailed FE models with shell and/or solid elements as well as more realistic geometry and material properties are used in order to dimension wound reinforcement structures appropriately. Thus, failure and damage evolution models can be evaluated in addition to elastic deformations. For instance, Krystek et al. [6] as well as Havar [7] generate and analyze macroscopic solid element models of filament wound loop specimens. By applying different failure criteria, they determine tensile breaking loads and failure areas. Botzkowski et al. [8] and Kärger et al. [9] increase the level of geometric detail by using a mesoscopic shell element model to analyze a filament wound reinforcement structure in an open-hole laminate. In order to model delamination effects, an isotropic separation layer is placed between the individually modeled windings (mesoscopic model). Failure initiation in the windings is evaluated according to the Hashin criterion [10], damage evolution is interpreted according to Lapczyk and Hurtado [11]. Depending on the curing conditions, thermosets and thermoset impregnated composites may contain significant residual stress and distortion which can have a considerable influence on their mechanical and geometric properties [12,13]. Methods for predicting the residual stresses and distortions in composites as a function of the curing conditions exist and are proven on different composite structures [14–18], but have not been yet applied in the structural simulation of 3D filament wound fiber skeletons.

The few existing publications that deal with such detailed FE simulations of wound reinforcement structures exclusively focus on thermoset impregnated skeletons. The present work aims to develop corresponding models for thermoplastic impregnated fiber skeletons, as these are predominantly manufactured and employed in context of the 3DSW technology. Based on experience from mechanical tests it can be assumed that leastwise the delamination behavior between the windings must be modeled more precisely. In order to obtain a generally applicable approach for detailed structural FE simulations of thermoplastic impregnated wound reinforcement structures, a systematic procedure of experimental tests and FE model set-up is proposed in this work.

2. General concept for validated FE modeling of fiber skeletons

Fig. 3 illustrates the proposed procedure to develop validated FE models for wound fiber skeleton structures. The structural constituents[1] typically occurring in fiber skeletons are impregnated rovings (A), metallic inserts (D) as well as the interface between two impregnated rovings (B) and the interface between an impregnated roving and an insert (C). In order to capture their mechanical behavior precisely, they are characterized in isolation by using appropriate mechanical test methods. Based on the results obtained, corresponding FE models of the structural constituents (*sub models*) are developed and parametrized. The next step is to integrate these sub models into a holistic FE model of a demonstrator skeleton (*main model*) which contains all considered structural constituents. The main model is validated by means of mechanical tests performed on the manufactured demonstrator skeleton. It represents a basic FE model for the mechanical analysis of thermoplastic impregnated fiber skeletons which is extensible to arbitrary geometries. If necessary, it can be refined by further investigations.

3. Design, manufacturing and mechanical testing of specimens

3.1. Design of specimens

The characterization of the structural constituents and the validation of the main model require specially adapted mechanical investigations. Table 1 gives an overview of the load types that can occur in each constituent and indicates the test specimens and test methods used to investigate them. In this work, the bending of impregnated rovings (which as part of a fiber skeleton are called *windings*) as well as the tangential shear between consolidated rovings (representing Mode II-delamination between adjacent windings) are focused, as they are known to be relevant implications of the mechanical loading of wound fiber skeletons [5,8,19].

As demonstrator skeleton, a simple loop structure is selected. It is easy to manufacture and has proved itself as a versatile specimen in context of 3D filament winding [5,6,20,21]. It contains all the consid-

[1] Structural constituents: phases within a structure showing clearly distinguishable mechanical properties

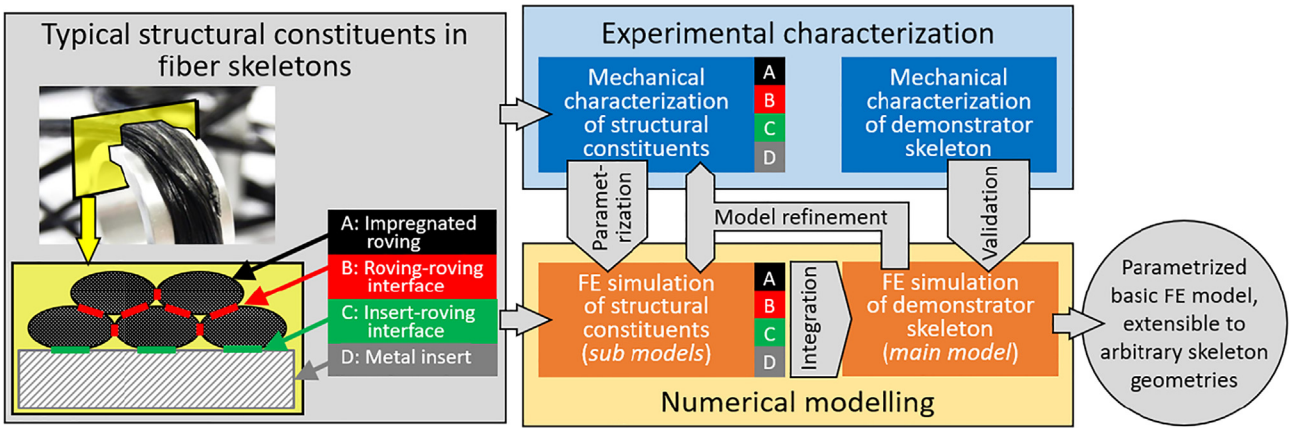

Fig. 3. Procedure for the development of a basic structural FE model for fiber skeletons.

Table 1
Potential load types and mechanical investigations for the structural constituents.

Structural constituents	Potential load types[1]	Mechanical testing method	Specimen
A (impregnated roving)	Bending	3-point-bending test	Impregnated roving
	Tension ||	The mechanical behavior under these load types is known from standard material characterization tests.	
	Tension ⊥		
	Compression ||		
	Compression ⊥		
	Shear ||⊥		
B (roving-roving interface)	Opening/tension (Mode I)	Not investigated in this work: Mode I-failure of the roving-roving interface is usually anticipated by Tension ⊥-failure in the adjacent rovings.	
	Sliding/shear (Mode II)	Lap shear test	Locally consolidated rovings (*weld seam specimen*)
C (insert-roving interface)	Opening/tension (Mode I)	Not investigated in this work: No significant adhesion can be observed between uncoated metal inserts and most thermoplastic impregnations.	
	Sliding/shear (Mode II)		
D (insert)	Compression	Not investigated in this work: The metal inserts generally show no significant deformation.	

[1]||: Parallel to fiber orientation, ⊥: transverse to fiber orientation.

ered structural constituents and is usually examined in tensile tests. Fig. 4 shows all specimen types used in the present work.

3.2. Materials and production of specimens

The material used for the production of all specimens is a commingled yarn consisting of unconsolidated E-glass fibers (GF) and Polypropylene filaments (PP). Its linear density amounts to 1870 tex (g/km), with a measured glass fiber content of 35% by volume. The commingled yarn was supplied by Owens Corning under the trade name *Twintex ® RPP60 1870B*.

The impregnated rovings for the 3-point-bending experiments are produced by using only the first step (*impregnation*) of the 3DSW process shown in Fig. 1. This procedure essentially corresponds to a pultrusion process using commingled yarns. The pultrusion die used has a round cross section with a diameter of 2 mm. In order to receive

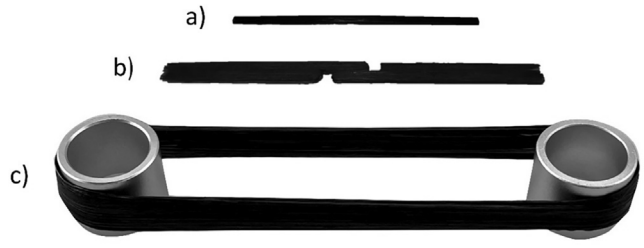

Fig. 4. Specimens – a) impregnated roving, b) weld seam specimen, c) simple loop skeleton.

specimens suitable for bending tests, the initially round rovings are subsequently pressed to a rectangular profile. The weld seam specimens are produced by compressing four of these pressed rovings in such a way as to produce test specimens similar to ISO 11003–2 [22]. Fig. 5a) shows the press tool used for the production of the impregnated rovings and the weld seam specimens. The simple loop skeletons are produced by using the first two steps (*impregnation* and *3D Winding*) of the 3DSW process. A manually guided hot air gun ensures that the windings are joined above the PP's melting point. The winding tool used for this purpose is shown in Fig. 5b). Loop skeletons of two and six windings are produced. The inserts in the simple loop skeleton are made from aluminum. The essential dimensions of all specimens are specified in Fig. 6.

In the structural FE simulations, the impregnated PP-GF rovings are considered as a unidirectional composite. Accordingly, their mechanical behavior is defined by transversely isotropic elastic constants and strength values. Since automated 3D filament winding processes are known to often involve a certain twisting of the reinforcement fibers, this represents an idealization of reality which must be kept in mind when interpreting the simulation results. As shown in [23], it may cause deviations regarding elastic deformation (stiffness) as well as maximum bearable load (strength). Nevertheless, this constitutes the current state of the art in the structural simulation of 3D filament wound fiber skeletons [6–9]. Most of the transversely isotropic material properties used in this work are determined by standard tests [24–26] on unidirectionally reinforced plate specimens which are produced in a vacuum consolidation process using the PP-GF commingled yarn. A few values which are not determined by standard tests are calculated by means of representative volume element (RVE) simulations

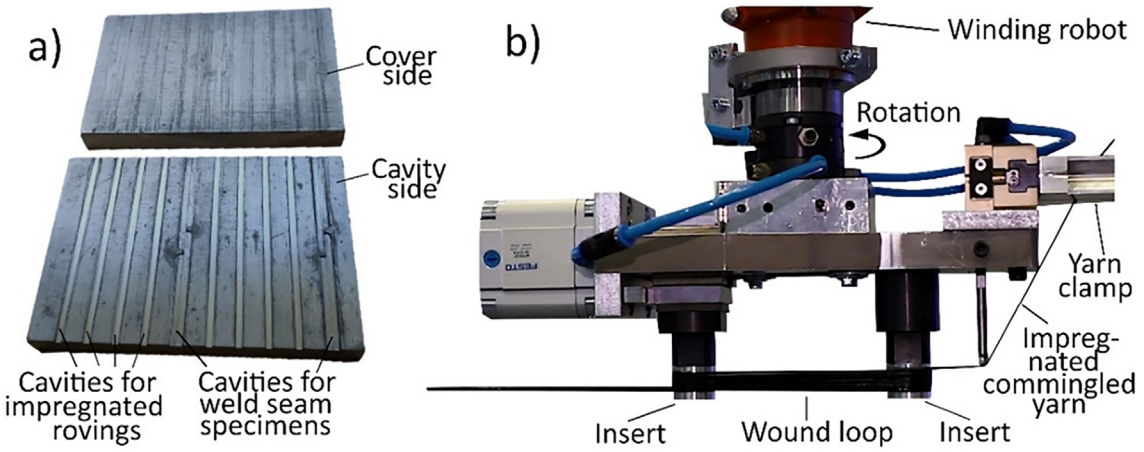

Fig. 5. Tools used to produce specimens – a) press tool for impregnated rovings and weld seam specimens, b) winding tool for simple loop skeletons.

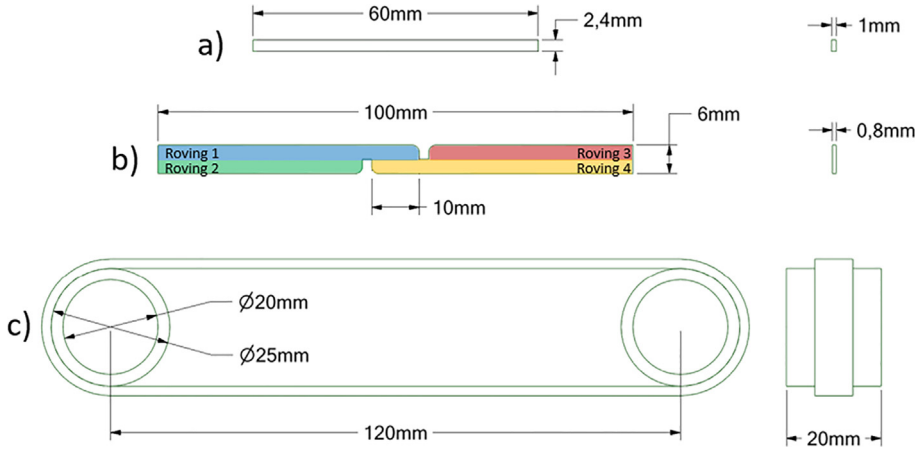

Fig. 6. Essential dimensions of the specimens - a) impregnated roving, b) weld seam specimen, c) simple loop.

Table 2
Transversely isotropic elastic constants and strength values of the PP-GF roving.

Elastic constants							
Parameter	$E_{\|\|}$ [MPa]	$E_{\perp}$ [MPa]	$G_{\|\|\perp}$ [MPa]	$G_{\perp\perp}$ [MPa]	$\nu_{\|\|\perp}$ [−]	$\nu_{\perp\|\|}$ [−]	$\nu_{\perp\perp}$ [−]
Determination	ISO 527–5	ISO 527–5	ASTM D 5379	RVE	RVE	RVE	RVE
Value	26,518	3750	1225	1125	0.32	0.32	0.59
Strength values							
Parameter[1]	$R_{\|\|t}$ [MPa]	$R_{\|\|c}$ [MPa]	$R_{\perp t}$ [MPa]	$R_{\perp c}$ [MPa]	$R_{\|\|\perp}$ [MPa]	$R_{\perp\perp}$ [MPa]	
Determination	ISO 527–5	ISO 14,126	ISO 527–5	ISO 14,126	ASTM D 5379	Analytical calculation	
Value	609.0	274.0	6.7	44.6	17.0	17.8	

[1]t: Tension, c: compression.

following Barbero et al. [27] or by analytical approaches following Schürmann [19]. The basic mechanical characterization of the impregnated PP-GF rovings is summarized in Table 2. Further material characterizations are part of the present work. As indicated in Table 1, the nonlinearities occurring during the bending of impregnated rovings and during the tangential shear of the roving-roving interface are modeled and parametrized based on experimental characterizations.

3.3. Mechanical testing of structural constituents and demonstrator skeleton

The 3-point-bending tests on impregnated rovings are conducted following DIN EN ISO 14125 [28] on a Hegewald & Peschke inspekt table blue 5 testing machine using a mechanical extensometer and a 500 N load cell. The test set-up is shown in Fig. 7 a). The test speed is set to 1 mm/min. The lap shear tests on weld seam specimens are performed at 23 °C on a Hegewald & Peschke inspekt table 50 testing machine using a video extensometer and a 500 N load cell. Fig. 7b) shows the test set-up used. In this case as well, the test speed is set to 1 mm/min. The simple loop skeletons are subjected to tensile tests which are carried out on the same machine as the lap shear tests. However, a 50 kN load cell is used and the test speed is set to 5 mm/min. The test set-up is shown in Fig. 7c). At least five experiments are performed per test series. The experiments are filmed with a Canon EOS 700D digital camera.

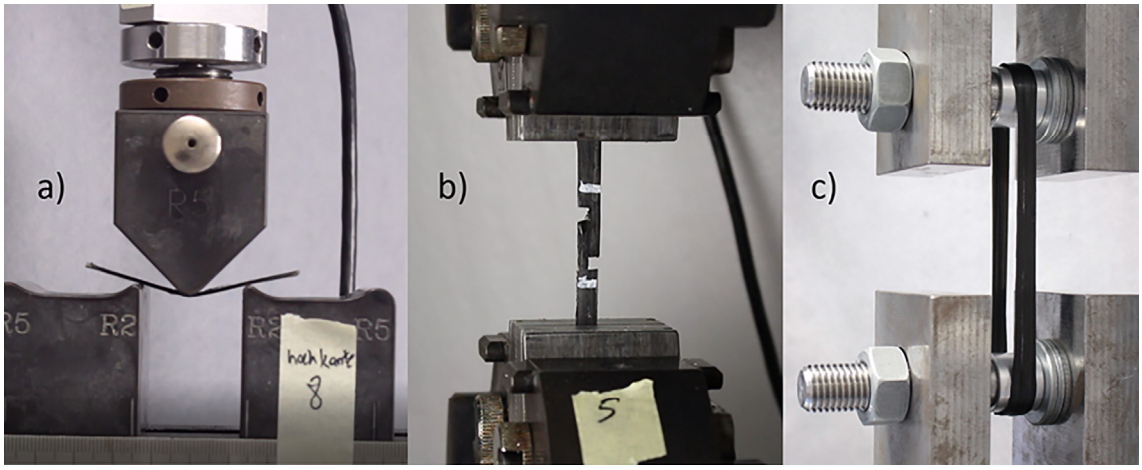

Fig. 7. Test set-ups – a) 3-point bending test on impregnated rovings, b) lap shear test on weld seam specimens, c) tensile test on simple loop skeletons.

4. Development and parametrization of finite element models

4.1. Material modeling of the impregnated roving

The elastic behavior of the impregnated roving is represented by the transversely isotropic elastic constants given in Table 2. To determine damage initiation within the impregnated rovings, both the Hashin [10] as well as the Maximum Stress criterion, given in the Eqs. (1)–(10), are applied in this work. The objective is to compare the precision of the two criteria by comparing their results with experimental data. Since the criteria cannot be applied simultaneously, separate simulations are carried out. In both cases, the strength values given in Table 2 serve as input. For comparison purposes, the Maximum Stress criterion is, in another separate simulation, also applied with the homogenized fiber-parallel tensile strength ($R_{||t}$) of 1232.2 MPa, which is obtained by applying the rule of mixture given in [19] with a fiber volume content of 35%, a glass fiber strength of 3450 MPa and a PP strength of 38 MPa.

Hashin criterion

Fiber tensile fracture ($\sigma_1 > 0$):

$$\frac{\sigma_1^2}{R_{||t}^2} + \frac{\tau_{12}^2 + \tau_{13}^2}{R_{||\perp}^2} = 1 \tag{1}$$

Matrix tensile fracture ($\sigma_2 + \sigma_3 > 0$):

$$\frac{(\sigma_2 + \sigma_3)^2}{R_{\perp t}^2} + \frac{\tau_{23}^2 - \sigma_2\sigma_3}{R_{\perp\perp}^2} + \frac{\tau_{12}^2 + \tau_{13}^2}{R_{||\perp}^2} = 1 \tag{2}$$

Fiber compressive fracture ($\sigma_1 < 0$):

$$\frac{\sigma_1^2}{R_{||c}^2} = 1 \tag{3}$$

Matrix compressive fracture ($\sigma_2 + \sigma_3 < 0$):

$$\left(\left(\frac{R_{\perp c}}{2R_{\perp\perp}}\right)^2 - 1\right)\frac{(\sigma_2 + \sigma_3)}{R_{\perp c}} + \frac{(\sigma_2 + \sigma_3)^2}{4R_{\perp\perp}^2} + \frac{\tau_{23}^2 - \sigma_2\sigma_3}{R_{\perp\perp}^2} + \frac{\tau_{12}^2 + \tau_{13}^2}{R_{||\perp}^2} = 1 \tag{4}$$

Maximum Stress criterion

Fiber tensile fracture:

$$\frac{\sigma_1}{R_{||t}} = 1 \tag{5}$$

Matrix tensile fracture:

$$\frac{\sigma_2}{R_{\perp t}} = 1 \vee \frac{\sigma_3}{R_{\perp t}} = 1 \tag{6}$$

Fiber compressive fracture:

$$-\frac{\sigma_1}{R_{||c}} = 1 \tag{7}$$

Matrix compressive fracture:

$$-\frac{\sigma_2}{R_{\perp c}} = 1 \vee -\frac{\sigma_3}{R_{\perp c}} = 1 \tag{8}$$

Fiber-parallel shear fracture:

$$\frac{|\tau_{12}|}{R_{||\perp}} = 1 \vee \frac{|\tau_{13}|}{R_{||\perp}} = 1 \tag{9}$$

Fiber-transverse shear fracture:

$$\frac{|\tau_{23}|}{R_{\perp\perp}} = 1 \tag{10}$$

σ_i and τ_{ij} represent the locally occurring normal and shear stresses, where the index 1 corresponds to the fiber orientation while the indexes 2 and 3 are perpendicular to it and perpendicular to each other (both transverse to the fiber orientation).

The Material Property Degradation feature (MPDG) implemented in *ANSYS Mechanical* is used to consider the impairment of the material properties which is caused by damage initiation. It can be applied in combination with the Hashin as well as with the Maximum Stress criterion. The theoretical approach underlying the MPDG feature is based on a degradation model proposed by Camanho and Matthews [29] which carries out instant stiffness reductions in those elements where damage initiation has been determined. The stiffness reductions are specific to the determined failure mode. Their definitions are given in the Eqs. (11)–(18):

Fiber tensile fracture:

$$E_{||}^d = (1 - D_{||t})E_{||} \tag{11}$$

Matrix tensile failure:

$$E_{\perp}^d = (1 - D_{\perp t})E_{\perp} \tag{12}$$

$$G_{||\perp}^d = (1 - D_{\perp t})G_{||\perp} \tag{13}$$

$$G_{\perp\perp}^d = (1 - D_{\perp t})G_{\perp\perp} \tag{14}$$

Fiber compressive fracture:

$$E_{||}^d = (1 - D_{||c})E_{||} \tag{15}$$

Matrix compressive failure:

$$E_{\perp}^d = (1 - D_{\perp c})E_{\perp} \tag{16}$$

$$G^d_{\|\perp} = (1 - D_{\perp c})G_{\|\perp} \tag{17}$$

$$G^d_{\perp\perp} = (1 - D_{\perp c})G_{\perp\perp} \tag{18}$$

$E^d_{\|}, E^d_{\perp}, G^d_{\|\perp}$ and $G^d_{\perp\perp}$ represent the degraded elastic constants applied in the damaged elements. $D_{\|t}, D_{\perp t}, D_{\|c}$ and $D_{\perp c}$ are the stiffness reduction factors that are adapted to the mechanical behavior of the impregnated rovings in this work. For this purpose, a curve fitting is carried out based on the measurements obtained in the 3-point bending tests described in 5.1.

4.2. Material modeling of the roving-roving interface

The mechanical behavior of the roving-roving interface is represented by a bilinear Cohesive Zone Model (CZM) implemented in *ANSYS Mechanical* which is based on Alfano and Crisfield [30]. The CZM specifies the relationship of the tractions τ and the separations δ between interface surfaces as shown in Fig. 8.

This CZM can be applied to Mode I, Mode II as well as Mixed-Mode loadings. However, as indicated in Table 1, only Mode II is considered in the present work. Therefore, the parameters to be specified are limited to the maximum tangential cohesive traction $\tau_{t,max}$, the tangential separation at completion of debonding $\delta_{t,d}$ and the tangential cohesive stiffness k_t. Their experimental determination is described in 5.2.

4.3. FE modeling of the 3-point bending tests on impregnated rovings

Like all FE models in this work, the model of the 3-point bending tests is designed using the CAD software *ANSYS SpaceClaim* and subsequently prepared, computed and analyzed using the commercial FE software *ANSYS Mechanical*. The impregnated roving is modeled as a profile with a rectangular cross section according to the dimensions given in Fig. 6. The material modeling of the impregnated roving is described in 4.1. The local coordinate system of each individual element is aligned according to the (idealized) fiber orientation within the impregnated roving. Thus, the correct orientation of the transversely isotropic material properties is ensured at every point. The roving is represented by SOLID186 elements. SOLID186 is a 20-node 3D solid element with a quadratic shape function and three degrees of freedom per node (translations in x, y and z direction). The three-point bending load is modeled by an assembly that includes the supporting/loading pins in the form of rigid bodies in addition to the roving. Fig. 9a) shows that symmetries are exploited by simulating only a quarter of the assembly. The roving and the pins are connected via frictionless contacts which only transmit compression. The load is applied by displacing the loading pin while the support pins are fixed.

4.4. FE modeling of the lap shear tests on weld seam specimens

The geometry of the weld seam specimen model is also based on the dimensions given in Fig. 6. However, the dimensions of the interface area are adjusted to 10.5 mm × 0.87 mm after measuring. Also, the long ends of the specimen are shortened in the model to reduce calculation time. The rovings are modeled as described in 4.3. The material modeling of the roving-roving interface is defined in 4.2. As shown in Fig. 9b), the thickness of the interface is neglected so that the consolidated rovings are in direct contact. The tensile load is applied by displacing one end of the specimen while fixing the other end.

4.5. FE modeling of the tensile tests on simple loop specimens

The simple loop specimens are modeled on mesoscopic level. Compared to the previously described specimens, the geometric modeling is less obvious in this case. The dimensions of the inserts and the distance between them can be taken from Fig. 6. However, it is a peculiarity of 3D filament wound structures that the cross-sectional shape of the windings as well as the contact area in between adjacent windings are difficult to describe geometrically and vary over the course of the loop. In order to still be able to perform detailed FE simulations of wound fiber skeletons, precise geometry approximations must be created. Initial observations show that the front side of the loops, marked (i) in Fig. 10b), differs from the back side, marked (ii), as it contains one more roving. This is due to the final overlap applied during the winding process. The bolt wrappings, marked (iii), are considered as a further characteristic area. It is assumed that both wrappings are identical. Fig. 10 also shows that the present work presents geometric models that consider the particularities of these three characteristic areas. Essentially, there are two geometrical properties, i.e. dimensions, which are considered to be particularly relevant with regard to the mechanical behavior of the simple loops and at the same time differ significantly in the characteristic areas (i), (ii) and (iii). The contact width between adjacent rovings, which has a significant influence on the delamination behavior focused in this work, and the thickness of the loop, which strongly affects its maximum load capacity [8]. While the contact width and the loop thickness are considered separately for (i), (ii) and (iii), the cross-sectional area of a single winding, considered here as the third mechanically relevant dimension, is assumed to be constant over the entire loop. It is specified with 2.47 mm^2 which corresponds to the total cross-sectional area of all GF and PP filaments contained in one winding. The transitions between (i) and (iii) as well as between (ii) and (iii) are modeled as straight-line connections. The described characteristics and dimensions are graphically explained in Fig. 10.

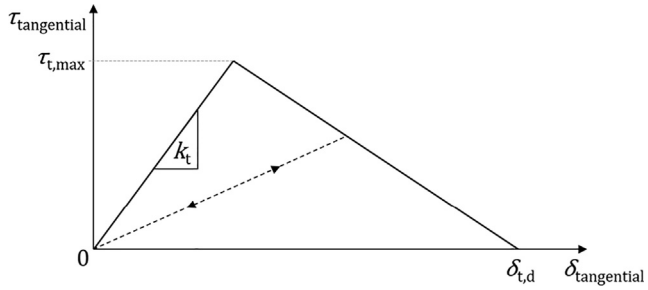

Fig. 8. Traction-separation relationship of a bilinear Mode II-CZM, modified from [30].

To quantify the contact width between adjacent windings and the loop thickness at (i), (ii) and (iii), two additional sets of loop specimens, with two and six windings respectively, are produced in this work. From these specimens, micrographs are generated with which the cross section of the wound loops can be analyzed. As shown in Fig. 11, small pieces of 0.05 mm Kapton foil are placed between the windings at (i), (ii) and (iii) during the winding process, so that the interfaces in between windings can be identified and measured in the micrographs. The measurements are made using the public domain image processing software *ImageJ*. To calculate the average contact width between two adjacent windings, the cumulative interface length in a micrograph is divided by the number of pictured windings minus one. The loop thickness is measured directly in the micrographs. The described approach generally allows measurements of the loop's cross section, but is not free of uncertainties due to the complex cross-sectional shapes which vary over the course of the loop. Table 3 gives an overview of the measurements made.

To simulate the tensile tests on the simple loop specimens, the geometric models shown in Fig. 10 are adapted according to the dimensions listed in Table 3. All windings are modeled with a rectangular cross section. Since the cross-sectional area of a single winding, the loop thickness and the winding numbers are known for (i), (ii) and (iii), the local height and width of the individual windings are clearly defined and easy to calculate. The material properties and orientations within the windings as well as the meshing are defined according to

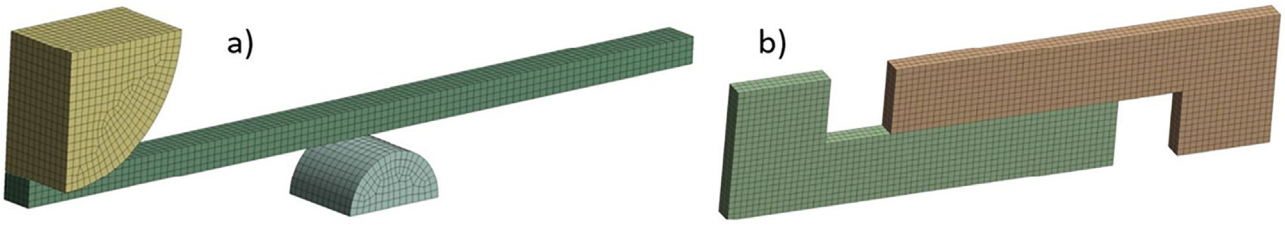

Fig. 9. FE sub models – a) the 3-point-bending test on impregnated rovings (quartered), b) the weld seam specimen (shortened).

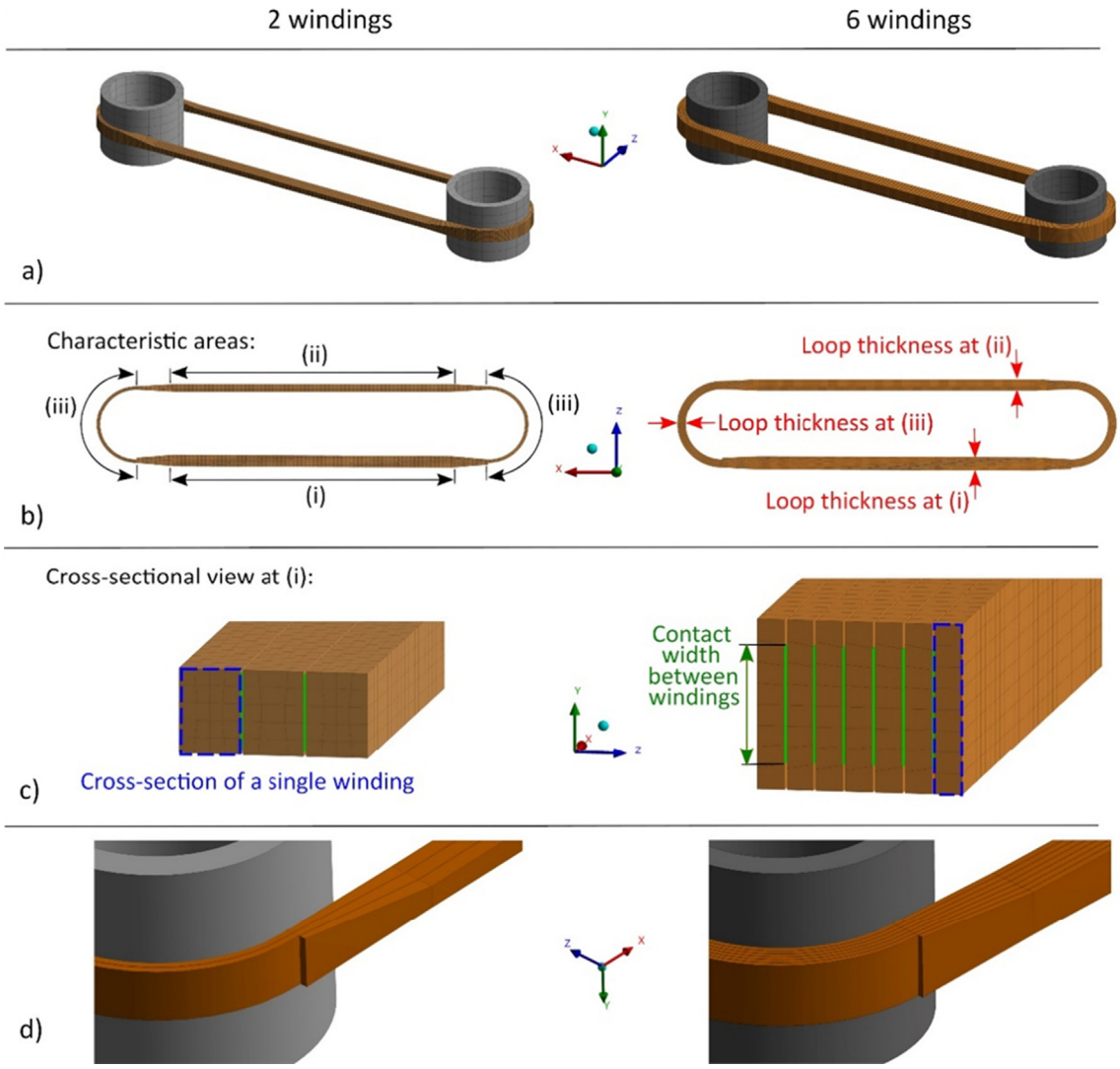

Fig. 10. FE main models for loop specimens with two and six windings – a) full models including inserts, b) top view, characteristic areas and local loop thickness, c) sectional view at (i), contact width between adjacent windings and cross-sectional area of a single winding, d) transition area between (i) and (iii).

the descriptions given in 4.1 and 4.3. Adjacent windings are in contact with each other over the entire winding length, i.e. either two or six windings. The length of the contact area thus directly depends on the number of windings. The width of the contact area is based on the average contact widths given in Table 3. The material modeling of the interface in between windings is defined according to the description in 4.2. Since no significant adhesion can be observed between uncoated metallic inserts and most thermoplastic impregnations and since no significant sliding is to be expected in the case of the tensile-loaded simple loop, the interface between the insert and the loop is neither characterized nor parameterized in this work. This contact is modeled as a frictionless contact which only transmits compressive forces. The tensile load is applied by displacing one insert while the other insert is fixed.

5. Experimental and numerical results

5.1. Three-point bending tests and parametrization of the impregnated roving

In the three-point bending experiments on impregnated rovings it is observed that the initial failure occurs at 15–20 N on the top side

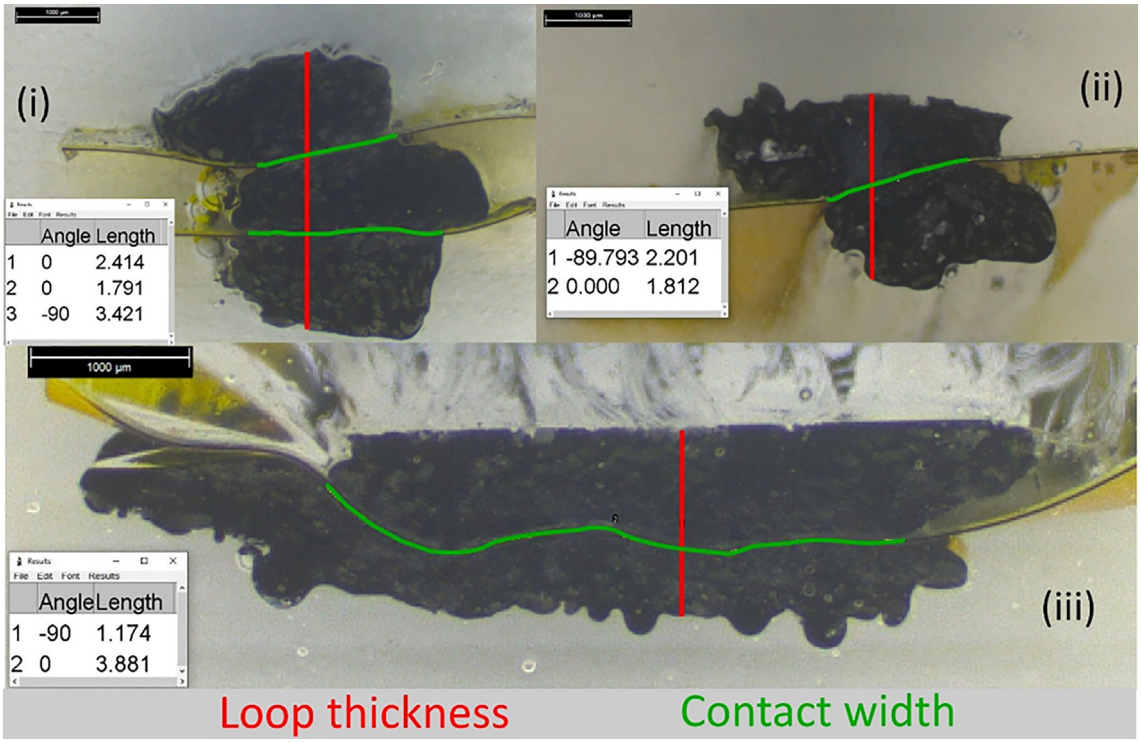

Fig. 11. Micrographs taken in the areas (i), (ii) and (iii) of a two-winding-loop, evaluation of the cross sections.

Table 3
Contact width and loop thickness measured on simple loop specimens with two and six windings.

Area	Simple loops with 2 windings		Simple loops with 6 windings	
	Avg. contact width (Std. Dev.) [mm]	Loop thickness (Std. Dev.) [mm]	Avg. contact width (Std. Dev.) [mm]	Loop thickness (Std. Dev.) [mm]
(i)	1.73 (0.51)	3.92 (0.83)	2.60 (0.63)	4.61 (0.66)
(ii)	1.46 (0.16)	2.62 (0.58)	2.95 (0.43)	3.45 (0.45)
(iii)	3.62 (0.71)	1.15 (0.10)	5.28 (0.34)	2.59 (0.20)

of the specimen where fiber buckling is caused by the compressive stresses acting there. The total failure occurs at an averaged maximum force of 25.4 N, as local tensile stresses on the bottom side induce fiber fracture. As displayed in Fig. 12, the force–deflection measurements take a linearly increasing course until the initial failure occurs. Due to the progressive damage evolution, a degressively increasing course follows which continues until total failure.

Fig. 12 also shows that the roving model described in 4.3 gives a good representation of the measured force–deflection curves. The calculated bending stiffness slightly overestimates the measured bending stiffness. Both, the maximum force calculated by the MPDG/Hashin combination as well as the maximum force calculated by the MPDG/Maximum Stress combination, are within the spreading width of the experimental results. The bending failure is mainly determined by the fiber-parallel compressive strength of the impregnated roving. At the time of the total failure, only about 8% of the damaged elements show fiber tensile fracture (bottom side), while the remaining ca. 92% show fiber compressive fracture (top side and middle area). The associated stiffness reduction factors, determined by a DoE-based curve fitting, are given in Table 4.

5.2. Lap shear tests and parametrization of the roving-roving interface

The tangential relative movement between the two welded rovings is largely linear. The twisting of the welded area typically occurring in lap shear tests is prevented by a short overlap and by a high geometrical in-plane bending stiffness. As shown in Fig. 13, the force–deflection curves initially rise linearly until they reach an averaged maximum force of 76.2 N. This is followed by a degressive decrease. The debonding of the welded rovings is completed at a deflection of about 0.5 mm. Based on the values obtained in the lap shear tests, together with the welded area of 9.1 mm^2, the CZM-Mode II parameters are determined, cf. Table 4.

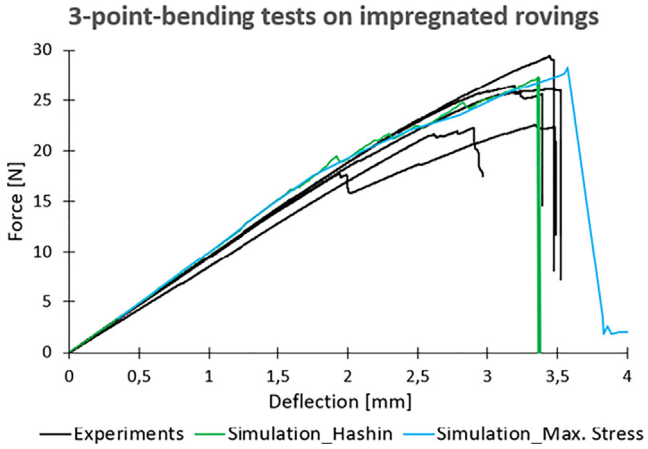

Fig. 12. Experimental and numerical results of the 3-point-bending experiments on impregnated rovings.

Table 4
MPDG-stiffness reduction factors for impregnated rovings and CZM-Mode II parameters for the roving-roving interface.

Material Property Degradation Method for impregnated rovings – Stiffness reduction factors				
Parameter	$D_{\|\|t}$ [−]	$D_{\|\|c}$ [−]	$D_{\perp t}$ [−]	$D_{\perp c}$ [−]
Determination	ISO 14125, DoE	ISO 14125, DoE	ISO 14125, DoE	ISO 14125, DoE
Value	1.00	0.64	0.13	0.10
Cohesive Zone Model for the roving-roving interface – Mode II parameters				
Parameter	$\tau_{t,max}$ [MPa]	$\delta_{t,d}$ [mm]	k_t [N/mm^3]	
Determination	Lap shear test	Lap shear test	Lap shear test	
Value	8.37	0.5	74.3	

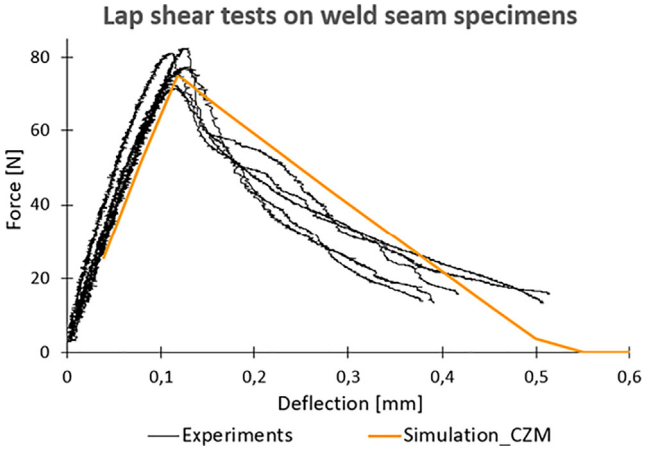

Fig. 13. Experimental and numerical results of the lap shear tests on weld seam specimens.

Fig. 13 also contains the curves generated by the weld seam specimen models described in 4.4. It can be seen that the CZM, based on the values listed in Table 4, gives a good representation of the measurements with the restriction that the course is linearized.

5.3. Tensile tests on simple loop specimens for experimental validation

Using the same commingled yarn as in this work, Huber [5] shows that the failure behavior of tensile-loaded simple loops varies depending on the number of windings. Loop specimens with two windings tend to fail by delamination and subsequent unwinding. In this failure mode, henceforth referred to as *interface failure*, the reinforcement fibers remain intact and only the matrix connecting the adjacent windings breaks. In contrast, loops with 25 windings fail by a clean *fiber fracture*. Consistent with Schürmann's theoretical analysis of wound composite loops [19], these fiber fractures usually occur in one of the four transition areas between (i) and (iii) or between (ii) and (iii). Loops with ten windings show a mixed failure pattern. Certain delamination processes do occur, but they are usually limited to a premature local detachment of the first and/or last deposited winding. The total failure of the loop occurs at a significantly higher elongation and is caused by fiber fractures in the remaining windings. As stated in [5], this variation of failure modes in dependency of the number of windings is related to the contact area between the windings. This area, and with it the adhesion between the windings, increases with the number of windings, which is why delaminations are less frequent at high winding numbers.

With regard to the two-winding-loops, the failure behavior quoted above matches partially with the experiments of the present work. One of the two-winding-loops actually fails by interface failure, i.e. complete delamination. However, the other four specimens, and thus the majority, show the mixed failure behavior. In this case, as shown in Fig. 16, first a local detachment of the first and/or last deposited winding occurs and later the remaining windings fail by fiber fracture. The fiber fractures occur at the transition between (i) and (iii) or between (ii) and (iii), as postulated in [19]. In the force–deflection measurements shown in Fig. 14, the mixed failure behavior is reflected by the fact that four of the measurement curves (*Experiments*) have two peaks. Video analyses show that the first peak indicates the local delamination while the second peak indicates the fiber fracture. In accordance with this, the measurement curve of the one specimen which failed by interface failure has only one peak.

The results of the FE model for the two-winding-loops, described in 4.5, strongly depend on the choice and the definition of the damage initiation criterion. The Hashin criterion leads to a clearly premature failure, as shown in Fig. 14 (green curve). The reason for this is that the Hashin criterion for fiber tensile fracture takes into account the locally acting shear stresses and relates them to the in-plane shear strength, cf. Eq. (1). As shown in Fig. 15, the in-plane shear strength given in Table 2 is exceeded at a relatively low tensile loading. This does not cause any recognizable failure in the experiments, but is evaluated as a fiber fracture by the Hashin criterion in the simulation. Given the low in-plane shear strength of the PP-GF composite material used in this work, which is presumably due to poor fiber–matrix adhesion, it can be assumed that the Hashin criterion is not ideal for the structural analysis of fiber skeletons made from this material. Hashin's consideration of shear stresses in the fiber tensile fracture criterion is controversial [31]. The Maximum Stress criterion for fiber tensile fracture does not consider shear stresses, so that much higher maximum forces are achieved (blue curve). However, even in this case, the simulation results remain behind the maximum forces achieved in the experiments and show fiber fracture instead of mixed failure behavior. One possible reason for this is that the fiber-parallel tensile strength ($R_{||t}$) listed in Table 2 is an experimentally determined value. In fiber-parallel tensile tests on unidirectionally reinforced composites, stress peaks usually occur at the clamping points, which leads to premature failure and thus to an underestimation of the material's strength [19]. The third variant of the simulation model (red curve) therefore uses the Maximum Stress criterion based on the homogenized fiber-parallel tensile strength of 1232.2 MPa, whose determination is described in 4.1. This significantly affects the result of the simulation which now shows the mixed failure behavior and therefore is in accordance with the observations from the tensile tests. Fig. 16 shows that the failure sequence in the simulation is the same as in the experiments. As shown in Fig. 14, there is also a good quantitative agreement between the measured and the calculated force–deflection curves. The maximum force is in the spreading width of the experimental results. Similar to the measurement curves, the calculated curve also shows a drop in force as a result of the local delamination. However, due to the moderate numerical damping of the CZM, which is necessary to avoid convergence problems, this drop is less abrupt. Regardless of the damage initiation criterion, the simulation model overestimates the stiffness of the loop specimens by ca. 25%, which causes an underestimation of the maximum elongation. This is probably due to process-related stiffness impairments. One aspect to be considered in this regard is the stiffness-reducing twist of fibers,

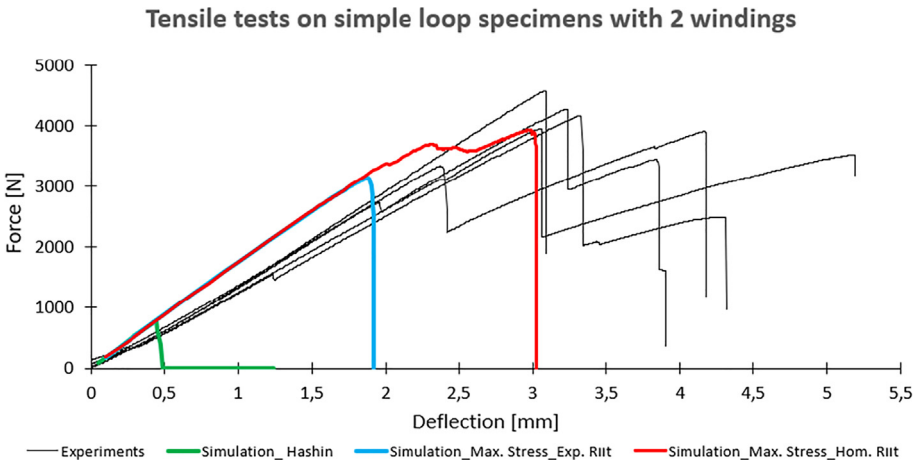

Fig. 14. Experimental and numerical results of the tensile tests on loop specimens with 2 windings.

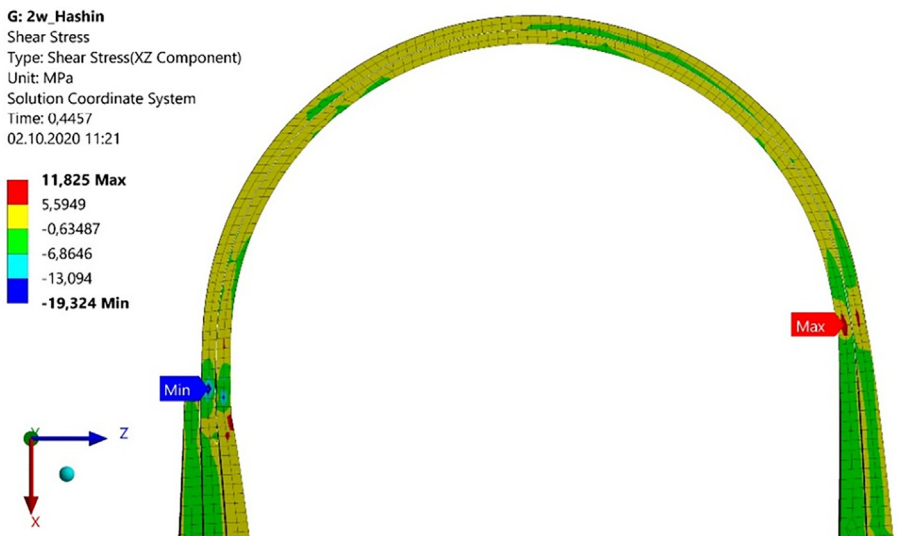

Fig. 15. Local shear stress in the two-winding-loop exceeding the in-plane shear strength at a tensile load of 788 N.

mentioned in 3.2, which can be observed in many fiber skeletons. The twisted fibers are not considered in the elastic constants in Table 2, since those were measured on vacuum-consolidated plate specimens. In this respect, the simulation results give an indication of the effect of the idealization made in 3.2, namely modeling the individual windings as a unidirectional composite, and thereby also point out respective potential for improving the presented simulation approach. Another potential aspect is that the windings are generally not symmetrically aligned in the area (iii), as shown in Fig. 11. This may intensify the slipping processes which are known to occur between windings deposited on top of each other in tensile-loaded wound loops [19], also resulting in a reduction of the loop's stiffness. This effect does not occur in the simulation models presented here, as the windings are modeled symmetrically.

The six-winding-loops show exclusively the mixed failure behavior. Again, the video analyses clearly show the two-stage failure consisting of local delaminations and fiber fractures. However, the delamination of a single winding has a smaller influence in this case. The percental reduction of the total contact area between the windings is much smaller compared to the loops with two windings. This is clearly recognizable by the force–deflection measurements in Fig. 17. The force drops caused by delamination are much smaller there than in Fig. 14.

The simulation of the six-winding-loops is also strongly influenced by the damage initiation criteria, cf. Fig. 17. As in the simulation of the two-winding-loops, the Hashin criterion and the Maximum Stress criterion, both based on the strength values listed in Table 2, result in premature fiber fracture. Again, the most precise results are determined by applying the Maximum Stress criterion with the homogenized fiber-parallel tensile strength. As depicted in Fig. 18, this simulation configuration yields, also here, a failure sequence which correctly represents the mixed failure behavior observed in the experiments. The quantitative agreement between the measured and the calculated force–deflection curves is similar to the two-winding-loops. In this case, the maximum force deviates by $<1\%$. The spikes caused by the delamination are only minimally pronounced in the calculated curve. The specimens' stiffness is overestimated by $+$ 28% which, also in this case, causes an underestimation of the maximum elongation.

6. Conclusion

The present work has demonstrated a systematic procedure of experiments and FE modeling steps enabling detailed and validated structural simulations of 3D filament wound fiber skeletons on mesoscopic level. Particular focus was placed on the individual winding

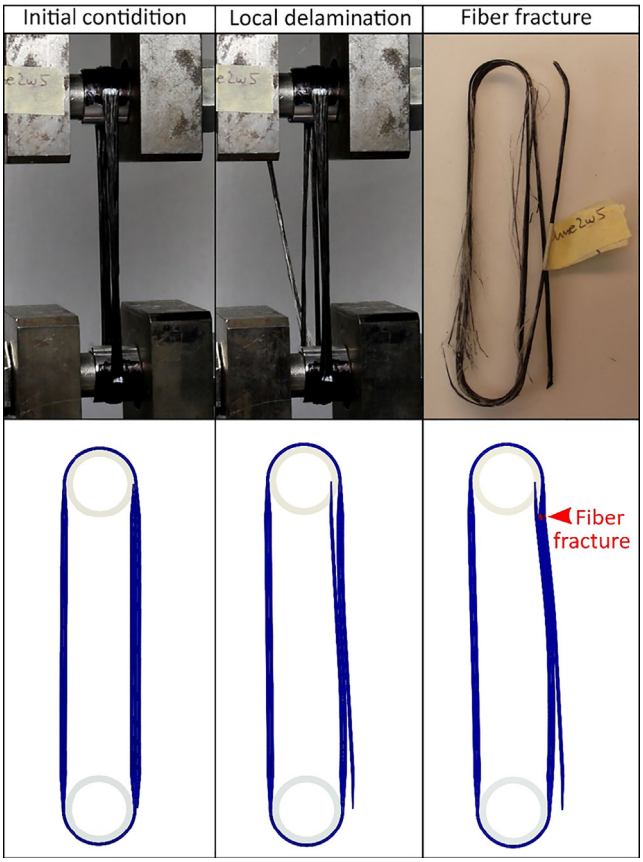

Fig. 16. Mixed failure behavior of the two-winding-loops in tensile tests (top) and simulations (bottom).

as part of the fiber skeleton, which essentially corresponds to an impregnated roving, and the interface between adjacent windings. To characterize the impregnated roving, extensive standard tests were carried out so that its elastic behavior, damage initiation (either by Hashin or Maximum Stress criterion) and damage evolution (Material Property Degradation Model) could be modeled and parameterized. In order to characterize the interface between two welded rovings (windings), an adapted lap shear test was carried out so that the deformation and failure behavior (Cohesive Zone Model) could also be modeled and parameterized in this case. The obtained models and parameters were then integrated into an FE model of a simple fiber skeleton – the wound loop. The wound loop was modeled with two and six windings, so that two separate FE models were created. In order to precisely approximate the local dimensions of the different loops, in particular the loop thickness and the contact area between adjacent windings, in the geometric models, micrographs were created and evaluated. The FE models were compared to the results of tensile tests on wound loop specimens. The best agreement between simulations and experiments was found by applying the Maximum Stress criterion and using a homogenized fiber-parallel tensile strength. With this configuration, the maximum bearable load could be calculated precisely. The delamination processes could also be reproduced, but only with a certain delay in stress reduction due to the numerical damping of the Cohesive Zone Model. The simulation models generally overestimated the stiffness of the loops, which was likely due to process-related stiffness impairments. It is assumed that the idealized modeling of the individual windings as a unidirectional composite with transversely isotropic elastic constants was the main cause for this stiffness overestimation, since this ignores the fiber twist which is known to frequently occur in 3D filament winding processes.

The procedure presented in this work can be transferred to other skeleton geometries as well as other composite materials and thus allows the creation of mesoscopic FE models for arbitrary fiber skeletons. As the interface between adjacent windings is modeled by means of a cohesive zone model, delamination processes, to which thermoplastic impregnations are susceptible, can also be precisely mapped. As also shown in [6] and [8], however, it should be noted that the geometric modeling of the fiber skeleton has a significant influence on the simulation results and therefore requires a high degree of precision. The methods of geometric analysis and measurement based on micrographs used in this work can only be applied if the examined fiber skeleton is already physically present as a specimen. Especially in the case of more complex fiber skeletons, this is associated with great effort. For such applications, methods are needed which allow a realistic and precise mesoscopic geometric modeling of fiber skeletons even before prototypes are produced. Possible starting points for this could be process simulations or parameter studies on the characteristic dimensions presented in this work. If the fiber skeleton is used as a local continuous fiber reinforcement of an injection molded part, however, the relevance of the geometric model's accuracy is supposedly reduced, since the embedding compound presumably reduces local delaminations. Another aspect that needs further research is the determination and modeling of the effective elastic behavior of wound fiber skeletons – considering process-related stiffness impairments such as fiber twists. In this respect, a first approach could be to determine the influence of different process and design factors on the elastic constants of wound impregnated rovings.

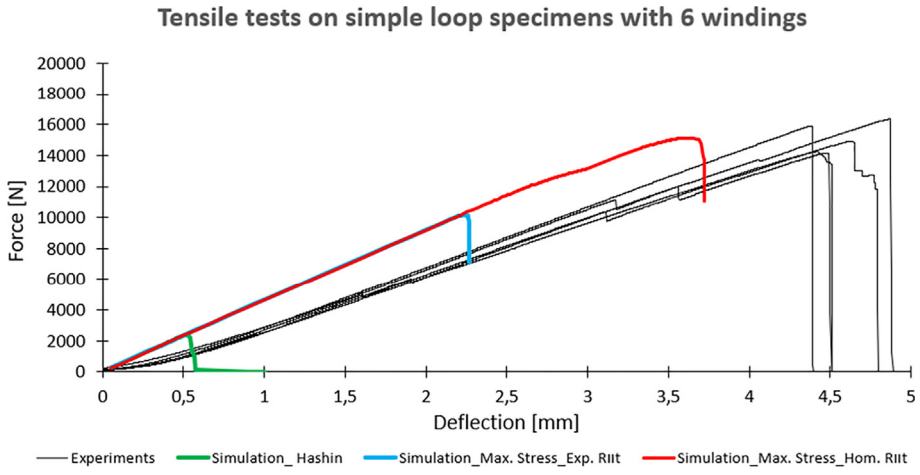

Fig. 17. Experimental and numerical results of the tensile tests on loop specimens with 6 windings.

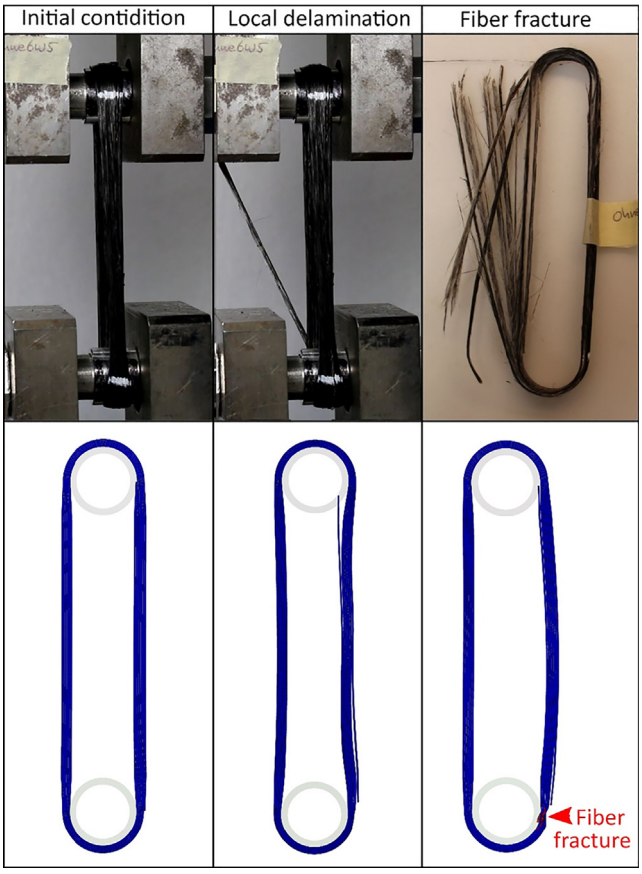

Fig. 18. Mixed failure behavior of the six-winding-loops in tensile tests (top) and simulations (bottom).

7. Data availability statement

The raw and processed data required to reproduce these findings cannot be shared at this time as the data also forms part of an ongoing study.

Declaration of Competing Interest

The authors declare that they have no known competing financial interests or personal relationships that could have appeared to influence the work reported in this paper.

Acknowledgements

The present work is part of the project ELeGanz-3D (Extremleichtbau durch ganzheitliches Engineering der 3D Skelett Wickeltechnik/ Extreme lightweight design through holistic engineering of the 3D Skeleton Winding technology). This project is funded by the research support program VIP+ (funding code: 03VP06670) granted by the German Ministry of Education and Research.

References

[1] Beck B, Tawfik H, Haas J, Park Y-B, Henning F. Automated 3D Skeleton Winding Process for Continuous-Fiber-Reinforcements in Structural Thermoplastic Components. In: Hopmann C, Dahlmann R, editors. Advances in Polymer Processing 2020. Springer, Berlin Heidelberg: Berlin, Heidelberg; 2020. p. 150–61.
[2] Morozov EV, Lopatin AV, Nesterov VA. Finite-element modelling and buckling analysis of anisogrid composite lattice cylindrical shells. Compos Struct 2011;93 (2):308–23. https://doi.org/10.1016/j.compstruct.2010.09.014.
[3] Minsch N, Müller M, Gereke T, Nocke A, Cherif C. 3D truss structures with coreless 3D filament winding technology. J Compos Mater 2018;53(15):2077–89. https://doi.org/10.1177/0021998318820583.
[4] Woods BKS, Hill I, Friswell MI. Ultra-efficient wound composite truss structures. Compos A Appl Sci Manuf 2016;90:111–24. https://doi.org/10.1016/j.compositesa.2016.06.022.
[5] Huber T. Einfluss lokaler Endlosfaserverstärkungen auf das Eigenschaftsprofil struktureller Spritzgießbauteile. Dissertation. Stuttgart: Fraunhofer Verlag; 2014.
[6] Krystek J, Kottner R, Bek L, Las V. Validation of the adjusted strength criterion LaRC04 for uni-directional composite under combination of tension and pressure. Appl Comput Mech 2010;4:171–8.
[7] Havar T. Beitrag zur Gestaltung und Auslegung von 3D-verstärkten Faserverbundschlaufen. Dissertation. Stuttgart: Institut für Flugzeugbau, Uni Stuttgart; 2007.
[8] Botzkowski T, Galkin S, Wagner S, Sikora SP, Kärger L. Experimental and numerical analysis of bolt-loaded open-hole laminates reinforced by winded carbon rovings. Compos Struct 2016;141:194–202. https://doi.org/10.1016/j.compstruct.2016.01.057.
[9] Kärger L, Botzkowski T, Galkin S, Wagner S, Sikora SP. Stress analysis and design suggestions for multi-loop carbon roving rosettes to reinforce bolt-loaded open-hole laminates. In: Proceedings ECCM17 - 17th European Conference on Composite Materials, 2016.
[10] Hashin Z. Failure criteria for unidirectional fiber composites. J Appl Mech 1980;47 (2):329–34. https://doi.org/10.1115/1.3153664.
[11] Lapczyk I, Hurtado JA. Progressive damage modeling in fiber-reinforced materials. Compos A Appl Sci Manuf 2007;38(11):2333–41. https://doi.org/10.1016/j.compositesa.2007.01.017.
[12] White SR, Hahn HT. Mechanical property and residual stress development during cure of a graphite/BMI composite. Polym Eng Sci 1990;30(22):1465–73. https://doi.org/10.1002/(ISSN)1548-263410.1002/pen.v30:2210.1002/pen.760302207.
[13] Kim KS, Hahn HT. Residual stress development during processing of graphite/epoxy composites. Compos Sci Technol 1989;36(2):121–32. https://doi.org/10.1016/0266-3538(89)90083-3.
[14] Abdelal GF, Robotham A, Cantwell W. Autoclave cure simulation of composite structures applying implicit and explicit FE techniques. Int J Mech Mater Des 2013;9(1):55–63. https://doi.org/10.1007/s10999-012-9205-7.
[15] Bogetti TA, Gillespie JW. Process-induced stress and deformation in thick-section thermoset composite laminates. J Compos Mater 1992;26(5):626–60. https://doi.org/10.1177/002199839202600502.
[16] Li D, Li X, Dai J, Xi S. A comparison of curing process-induced residual stresses and cure shrinkage in micro-scale composite structures with different constitutive laws. Appl Compos Mater 2018;25(1):67–84. https://doi.org/10.1007/s10443-017-9608-6.
[17] Dai J, Xi S, Li D. Numerical analysis of curing residual stress and deformation in thermosetting composite laminates with comparison between different constitutive models. Materials (Basel) 2019;12(4):572. https://doi.org/10.3390/ma12040572.
[18] Ding A, Li S, Sun J, Wang J, Zu L. A comparison of process-induced residual stresses and distortions in composite structures with different constitutive laws. J Reinf Plast Compos 2016;35(10):807–23. https://doi.org/10.1177/0731684416629764.
[19] Schürmann H. Konstruieren mit Faser-Kunststoff-Verbunden. 2nd ed. Berlin - Heidelberg: Springer Verlag; 2007.
[20] Minsch N, Müller M, Gereke T, Nocke A, Cherif C. Novel fully automated 3D coreless filament winding technology. J Compos Mater 2018;52(22):3001–13. https://doi.org/10.1177/0021998318759743.
[21] Büttemeyer H, Gosler A, Herrmann AS. Einfluss der Faservorspannung während der Aushärtung auf das quasi-statische Zugfestigkeitsverhalten von CFK-Schlaufenstrukturen. In: Tuchel J, editor. Textiltechnik als Schlüsseltechnologie der Zukunft: Tagungsband zur 15. Chemnitzer Texiltechnik-Tagung 31. Mai und 1. Juni 2016. Chemnitz: Technische Universität Chemnitz Professur Fördertechnik; 2016, p. 239–246.
[22] ISO 11003-2:2019-06. Adhesives - Determination of shear behaviour of structural adhesives - Part 2: Tensile test method using thick adherends.
[23] Minsch N, Herrmann FH, Gereke T, Nocke A, Cherif C. Analysis of filament winding processes and potential equipment technologies. Procedia CIRP 2017;66:125–30. https://doi.org/10.1016/j.procir.2017.03.284.
[24] DIN EN ISO 527-5:2010-01. Plastics - Determination of tensile properties - Part 5: Test conditions for unidirectional fibre-reinforced plastic composites.
[25] DIN EN ISO 14126:2000-12. Fibre-reinforced plastic composites - Determination of compressive properties in the in-plane direction.
[26] ASTM D5379 / D5379M - 19 Standard Test Method for Shear Properties of Composite Materials by the V-Notched Beam Method.
[27] Barbero EJ. Finite element analysis of composite materials using ANSYS. 2nd ed. Boca Raton, Fla: CRC Press; 2014.
[28] DIN EN ISO 14125:2011-05. Fibre-reinforced plastic composites - Determination of flexural properties.
[29] Camanho PP, Matthews FL. A progressive damage model for mechanically fastened joints in composite laminates. J Compos Mater 1999;33(24):2248–80. https://doi.org/10.1177/002199839903302402.
[30] Alfano G, Crisfield MA. Finite element interface models for the delamination analysis of laminated composites: mechanical and computational issues. Int J Numer Meth Eng 2001;50(7):1701–36. https://doi.org/10.1002/(ISSN)1097-020710.1002/nme.v50:710.1002/nme.93.
[31] Puck A. Ein Bruchkriterium gibt die Richtung an. Kunststoffe 1992;82(7):607–10.